Oblique injection depth correction by a two parallel OCT sensor guided handheld SMART injector

JINTAEK IM AND CHEOL SONG[*]

Department of Robotics Engineering, DGIST, 333 Techno Jungang-Daero, Daegu, 42988, Republic of Korea
[*]*csong@dgist.ac.kr*

Abstract: We present a SMART injector with two parallel common-path optical coherence tomography fibers to enable angle measurements and injection depth corrections for oblique subretinal injection. The two optical fibers are attached to opposite sides of a 33 G needle with known offsets and designed to pass through a 23 G trocar that has an inner diameter of 0.65 mm. By attaching a SMART system to a rotational stage, the measured angles are calibrated for minimal error from reference angles. A commercial eye model was used to evaluate the control performance, and injection experiments were performed on a phantom made of agarose gel and a porcine eye.

1.   Introduction

Subretinal injections are important ophthalmic procedures for various types of treatments in pharmacologic or genetic therapies [1–3]. In particular, several retinal gene therapeutic materials are injected in the eye as viral vectors to elicit expressions in the photoreceptor or retinal pigment epithelial (RPE) layer as promising methods to cure several retinal disorders [4,5]. For such operations, surgeons usually puncture the sclera with three surgical trocars that are then used for the surgical tool, illuminating probe, and irrigation tube, where the incision points are adjacent to the limbus [6]. Then, a microcannula is passed through the trocar, and its tip is inserted in the subretinal space under a targeted lesion to transplant drugs [7]. During the subretinal injection, the microcannula must be maintained stably inside the subretinal space for safety such that it does not penetrate the choroid beyond the retina [8]. In addition, the surgical trocar needs to be as stationary as possible along the transverse direction to prevent injuries, but it necessitates an inevitable oblique insertion into the retina because of the relative position between the trocar and a limited surgical lesion [9,10]. Meanwhile, oblique insertion is even beneficial for efficiency of injection as it prevents leakage of a drug or intraocular hemorrhage [11,12]. As an example, a parallel robot-assisted retinal microvascular stenting was implemented [13] that showed that the insertion angle of the guide wire had to be less than 46° in order to prevent puncturing the target vessel. In addition, the first subretinal injection aided by parallel robot was suggested in 1997 by using six DC servo motors and hydraulic actuator [14]. In the case of a hand-held type robot for subretinal injection, the physiological hand tremor has a root-mean-squared (rms) amplitude of 182 μm and 7 to 13 Hz frequency, which can cause excessive injection depth during a procedure [15]. The Micron was proposed as one of the hand-held devices for hand tremor compensation [16]; it uses a monocular camera to detect the position and orientation of the tool tip of the Micron and six small piezo motors to achieve control. Although this tool could be utilized to perform retinal cannulation [17], it is impossible to directly measure the relative position between the tool tip and the target sample.

Optical coherence tomography (OCT) is a technique capable of capturing a cross-sectional profile of a sample with a resolution of several micrometers [18], and it has been adopted to the

hand-held micromanipulator, smart micromanipulation aided robotic-surgery tool (SMART), along with an optical fiber in a common path (CP) manner and a linear piezo motor [19–21]. Recently, the SMART micro-injector system has been used to inject drugs at a target depth within a sample [22]. This tool provides good performance for hand tremor compensation during injection in a gelatin sample and a bovine eye, with rms errors of less than 5 μm and 11 μm, respectively; these values are much smaller than the thinnest sublayer of the retina, which is approximately 30 μm [23]. However, it is impossible to estimate the insertion angle, so the inclination of the needle cannot be considered when the injector is tilted with respect to a sample, which would introduce imprecise injection given a desired depth.

As a method for an angle measurement using a laser, an interferometer that illuminates two parallel rays on a sample could be used to calculate the angular displacement from the two measured positions [24,25]; those methods have been generally utilized for the calibration of a nanometer positioning stage. In this work, a SMART injector with two parallel CP-OCT fibers is developed for oblique subretinal insertion. The two CP-OCT fibers are utilized to measure both the distance to a target and the insertion angle, and a single piezo motor is actuated to control the position of a needle tip during distance-locking and injection.

2.   Materials and methods

2.1.   System configuration

As shown in Fig. 1(a), an OCT engine includes a swept-source laser with a central wavelength of 1060 nm and sweeping rate of 100 kHz (Swept Laser OEM engine, AXSUN), in addition to a photodetector. The illuminated light from the laser source is divided using a 2×2 coupler (TW1064R5A1A, Thorlabs) and relayed to the two optical fibers. Most of the optical configuration is the same as that suggested previously for the dual-OCT SMART system [26]. The presented system also introduces common-path scheme, so that back-reflected beam from the end surface of each fiber functions as a reference arm. To avoid interference between back-reflected beams from the two fiber ends, the two optical path lengths are separated by 1 m, which is much longer than the coherence length of the laser source. The main difference in this work is that both fibers are located to the needle, and a polarization controller (FPC024, Thorlabs) is added to remove the static fringe signal from the two distal ends of the fibers by altering the polarization states. The acquired fringe is digitized and transmitted to a frame grabber (PCIe-1433, National Instruments), which is built into a workstation (Precision T7610, Dell). Most of the data processing is performed by the graphics processing units (GPU, GeForce GTX1060, Nvidia) to rapidly analyze data using the computing unified device architecture (CUDA) protocol. Then, the control input is applied from the motor controller (PMD101, PiezoMotor) through an RS232 communication channel, and a piezoelectric linear motor (LEGS-LL1011A, PiezoMotor) is actuated to manipulate the position of the needle tip. Lastly, the Visual C++ based Microsoft foundation class (MFC) library was used to build a graphical user interface via Visual Studio 2019.

Figure 1(b) shows an image of the 33 G needle which has an outer diameter of 0.21 mm on the *xy* plane where the two CP-OCT fibers are attached to the opposite sides of the needle. These fibers are precisely aligned under observation with a portable microscope (Dino-Lite Edge, AnMo Electronics Corporation) and fixed by curing an ultraviolet (UV) epoxy. The first fiber is the one that is located closer to the needle tip; therefore, the diverged beam diameter at the needle tip from the first fiber is smaller than that from the second fiber, as shown in Fig. 1(c), which is obtained on the *xz* plane. Even though the two fibers are placed on the opposite sides of the needle, it is necessary to confirm if the reflected light from one fiber enters the other, i.e., if cross-talk exists.
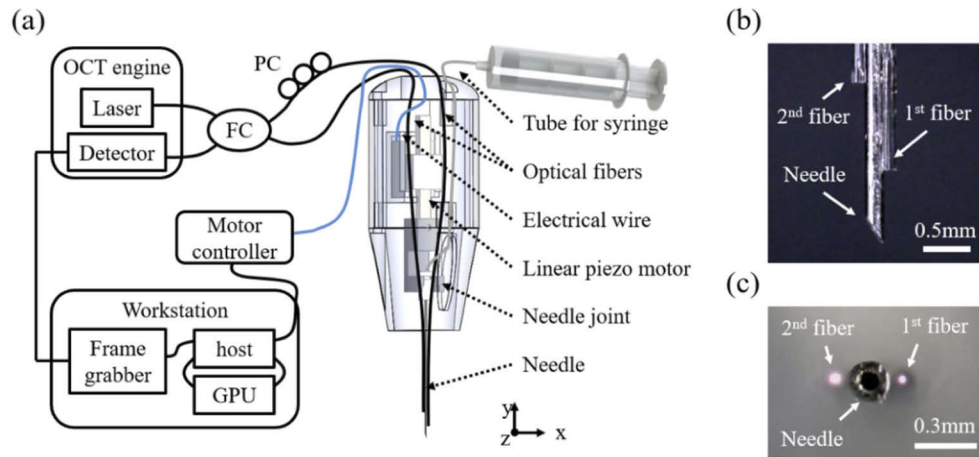
Fig. 1. Two parallel CP-OCT fibers attached SMART system. (a) System configuration: fiber coupler (FC), polarization controller (PC); (b) and (c) microscopic images of the two fibers attached to the needle along *xy* and *xz* planes, respectively.

2.2. Cross-talk test and algorithm for dual edge extraction

To observe the existence of cross-talk between the fibers, a specific optical configuration was designed, as shown in Fig. 2(a). An illuminated light from a laser is delivered to the two optical circulators using a 2×2 coupler. The circulators are connected to the 1st and 2nd fibers for position measurement and also transfer the reflected light to another 2×2 coupler. In addition, the distances to a sample from the two sources are denoted as d_{1st} and d_{2nd}, respectively. By connecting and disconnecting the joints j1 and j2, it is possible for the detector to selectively measure the signal from each fiber. Before the sample is placed within a detectable range, a total of 100 A-lines are averaged and removed from the raw A-line for background subtraction. Figure 2(b) shows the acquired A-line from a paper sheet, and the blue line is the total signal when both joints are connected; on the other hand, the red and green lines represent the signal that is acquired from either the 1st or 2nd fiber, respectively. The red and green signals do not contain sample signals from the other; thus, there is no cross-talk in this configuration. The part of the needle between the ends of the two fibers would prohibit light illuminated by one fiber from entering the other.

Figure 2(c) shows the algorithm for the dual edge detection; the red line indicates the A-line after background removal, and the blue line is a processed A-line that is acquired by low-pass filtering and thresholding. The acquisition rate of A-line is 1 kHz, and a central moving average is applied by using thirteen samples including a central data point and twelve adjacent data points. As a threshold, 10% of maximal intensity of A-line is used. To reliably extract the two edges of each fiber, the 1st and 2nd signal packets are selected to have prominent surface profiles of the sample in the following order. First, the notations 1st and 2nd indicate the individual fibers, and each of the initial boundaries is determined at the crossing point with the corresponding thresholds. Then, the 1st and 2nd final boundaries are selected to have pre-offsets from their initial boundaries. In this work, the two offsets are selected to be 200 μm and 300 μm, respectively. Within these boundaries, each peak is detected and the peaks become the distal ends of each signal packet. The proximal boundaries of both signal packets are determined by choosing the depth index that has a larger amplitude between those of the 1st initial /2nd final boundaries and 80% of each maximum peak from the corresponding signal packets. This boundary selection of both signal packets is applied to prevent a misdetection of each surface, such as the wrong
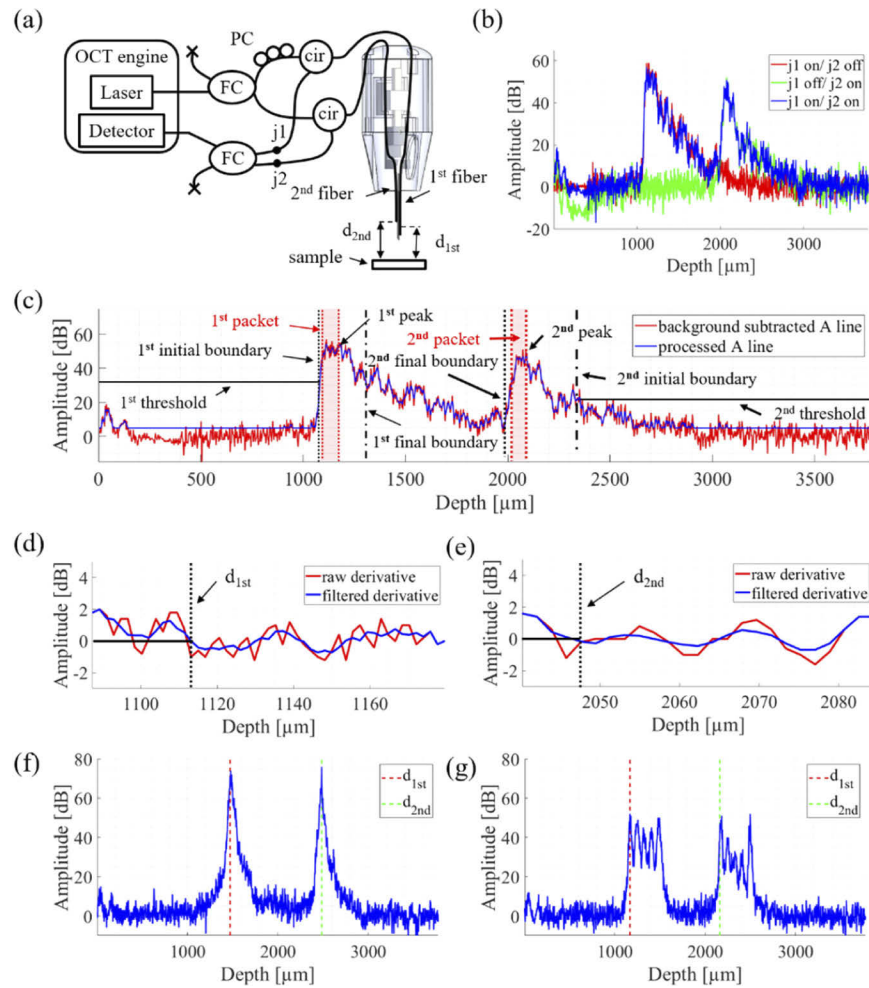
Fig. 2. Cross-talk test and dual edge detection algorithm. (a) Schematic of a test to confirm the existence of cross-talk: optical circulator (cir) and joints 1 and 2 (j1, j2); (b) resultant A-lines for cross-talk test; (c) typical A-line after preprocessing and dual signal packet detection parameters; (d) and (e) derivatives of the 1st and 2nd signal packets and their edge detection algorithms, respectively; (f) and (g) results of dual edge detection algorithm on aluminum plate and stacked cellophane tape.

edges by the noise. After taking the derivative on both signal packets, a central moving average filter is applied as a low pass filter by using five samples to reduce the noise. Then, zero-crossing points are detected to indicate the edges of the acquired A-line, as shown in Figs. 2(d) and (e). The depth indexes of the edges indicate the distances to the surface of the sample [27]; thus, they are designated as d_{1st} and d_{2nd} to calculate the position and angle of the needle tip from the sample. Figures 2(f) and (g) show the capability of dual edge detection algorithm on both single-layered and multi-layered samples. For the single-layered sample, an aluminum plate is used, and 4-stacked cellophane tape is introduced as a multi-layered sample. As indicated by red and green dotted lines, two edges from the sample surface are successfully detected by our algorithm. No matter what the sample profile is, the two signal packets show the same tendencies, and the dual edge detection algorithm extracts the first edge which is the sample surface.

2.3. Calibration and optimization for measured angle

In Fig. 3(a), the schematic of the parameters for angle calculation is described. First, d_{c2c} represents the distance between the cores of the fibers along the perpendicular axis to the main axis, and this is the sum of the outer diameters of the needle (0.21 mm) and the attached optical fibers (0.125 mm). Then, d_{gap} is noted as the distance between the two ends of the fibers along the main axis, which can be measured by subtracting d_{1st} from d_{2nd} when the needle is perpendicular to the sample. When the needle and fibers are aligned, d_{gap} is set to 1 mm to obtain an affordable range of angle measurements.

When d_{gap} is sufficiently small, the two signal packets are easily merged even for a small amount of inclination toward obtuse angles; moreover, a large d_{gap} precludes angle measurements when the needle is inclined at an acute angle because of the limited detection range of the OCT (3.7 mm) and weakened signal-to-noise ratio (SNR) of the 2nd edge. The variable $pos1$ represents the position of the needle tip with respect to the target sample, and d_{offset} is the distance from the needle tip to the end of the 1st fiber. During the injection, the needle tip should be inside sample and the 1st fiber is attached apart from the needle tip to enable measurement by 800 μm, in this study. Accordingly, $pos1$ has negative values during the injection. On the contrary, the distances of the 1st and 2nd fiber ends from the sample surface need to have positive values for measurement. The distances, d_{1st} and d_{2nd}, can be converted to the positions, $pos1$ and $pos2$, by subtracting d_{offset}. Therefore, $pos2$ is the virtual position of the 2nd fiber when it is translated toward the needle tip by d_{offset} to have the same d_{gap} value. Thus, $pos1$ and $pos2$ are expressed by the following equations.

$$pos1 = d_{1st} - d_{offset} \tag{1}$$

$$pos2 = d_{2nd} - d_{offset} \tag{2}$$

The position of the needle tip can be negative during injection, and all distances may always have positive values. When the needle is tilted by θ, the difference between the measured positions from each fiber deviates from d_{gap}, and the amount of this deviation is described as $d_{shifted}$. Here, $d_{shifted}$ and θ can be expressed by the following equations.

$$d_{shifted} = pos2 - (pos1 + d_{gap}) \tag{3}$$

$$\theta = 90° - \tan^{-1}\left(\frac{d_{shifted}}{d_{c2c}}\right) \tag{4}$$

The angle θ can be derived using trigonometry on the generated triangle in Fig. 3(a), and all values except d_{gap} and d_{c2c} can be updated while the system is operated. Here, d_{gap} and d_{c2c} are the parameters for angle calculation, and it is necessary to optimize them to minimize errors in angle measurements.

Figure 3(b) is the schematic for the angle calibration procedure. The SMART injector is connected to a rotational stage and measures a pitch angle on the *xy* plane, θ. The same microscope
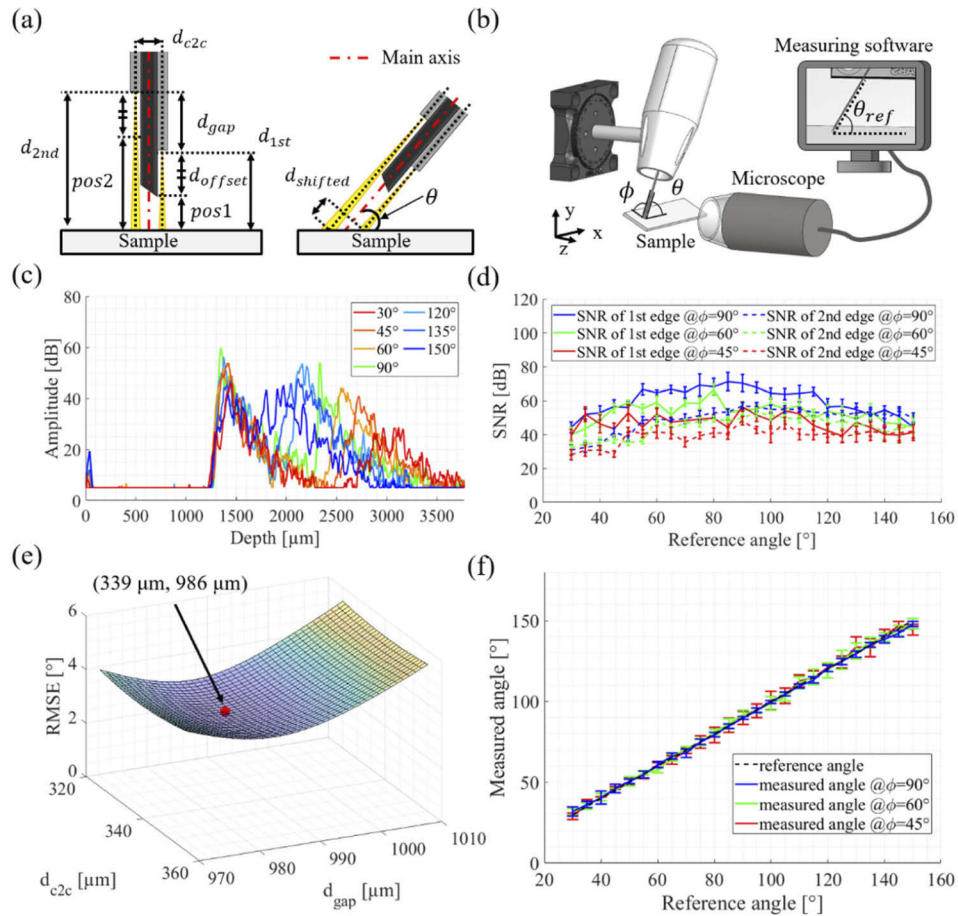
Fig. 3. Calibration and optimization of the parameters for angle calculation. (a) and (b) schematics of the parameters for angle calculation and calibration, respectively; (c) multiple A-lines at different reference angles; (d) signal-to-noise ratio (SNR) of the detected 1st and 2nd edges; (e) result of optimization of the parameters for angle calculation; (f) result of angle measurement after the calibration and optimization.

that is used for fiber alignment is placed in front of the stage, and the internal angle measurement software is used to obtain the reference angles, θ_{ref} for the angle calibration. Moreover, the roll angle on the yz plane, ϕ, was manipulated by 90°, 60°, and 45°. Our system was designed to measure the pitch angle on a xy plane which is generally visualized during an ophthalmic operation. The analysis on the roll angle is conducted to verify that geometrical inclination on another plane does not affect the measured angle, θ. Figure 3(c) shows seven A-lines that are captured on a paper sheet as the sample when the roll angle is 90°. Once the needle is inclined on the xy plane, the SNR worsens, and this was analyzed for both the 1st and 2nd edges, as shown in Fig. 3(d). It is noted that the SNR decreases when it deviates from both the reference angle and roll angle of 90°. In addition, it is difficult to reliably extract the edge of the 2nd packet when the needle is inclined at 30° or 150° owing to the broad widths and merged profiles of the signal packets.

To calculate the angle more accurately, an optimization procedure was performed to find the optimal values of d_{gap} and d_{c2c}. d_{1st} and d_{2nd} are saved during the calibrating procedure, and the angles are calculated using Eq. (4). Here, the grids of both d_{gap} and d_{c2c} for the optimization are generated (1 $\mu m \times 1$ μm), the root-mean-squared errors (RMSEs) between each calculated and reference angles are plotted, as shown in Fig. 3(e). The least RMSE value detected for d_{c2c} is 339 μm and that for d_{gap} is 986 μm. Figure 3(f) shows the calibration result after optimization of the parameters. The angles are calculated from 30° to 150° with 5° increments for three repetitions, and the black dotted line is the reference line for the measured results. The RMSEs of the measured angles are 1.14°, 1.22°, and 1.69° for ϕ values of 90°, 60°, and 45°, respectively. Then, the maximal RMSEs at each ϕ value are 2.97°, 2.59°, and 5.54°. In addition, the average of standard deviations of the measured angles are 1.87°, 2.84°, and 3.39° for each ϕ values. The maximal standard deviations at each ϕ value are 3.97°, 5.68° and 6.32°. When ϕ gets inclined, the accuracy of the angle measurements is degraded, however, the results are still well fitted with the reference angles.

2.4. Flow chart

Figure 4(a) explains the flow chart of the two parallel CP-OCT fibers attached SMART injector system. A total of 80 spectra of 1376 data points each are read framewise and transferred to the host spectrum buffer. Then, the device memory at the connected GPU allocates the spectrum buffer to handle those spectra and takes the data in the host spectrum buffer. The 80 spectra are averaged by 4, resulting in 20 averaged spectra, and zero padding is applied to increase the number of data points for one spectrum from 1376 to 4096. This enables obtaining 2048 data points in the resultant A-line while acquiring a half of a fast Fourier transform spectrum. Then, the 20 A-lines are averaged for robust edge detection. Thereafter, the single A-line is returned to the host memory; then, the two positions, $pos1$ and $pos2$, are extracted after background subtraction and A-line processing, as explained in Figs. 2(c)-(e).

From these values, the angle θ is calculated using Eq. (4), and the controller takes $pos1$ and θ for distance-locking and injecting procedures. The proportional controller is iterated for $pos1$ to have the desired value d_{des} by rejecting the hand tremor and modifying the control gain adaptively to obtain the least RMSE between $pos1$ and d_{des} by monitoring temporally averaged RMSE for 0.5 s. Finally, the control input is plugged into the motor driver and the procedures are operated every 1 ms, which is 50 times faster than the physiological hand tremor. Figure 4(b) shows the three different operating modes of our system. The first mode is freehand and starts analyses as soon as the system starts obtaining the spectra from the OCT engine. In the freehand mode, $pos1$, $pos2$, and θ can be manipulated freely as well as displayed and recorded. It is necessary for the needle to be moved in the vicinity of the sample to enable measurements by the two OCT sensors. Second, the motor is actuated to maintain the distance from the sample for d_{des} by the controller. This mode allows users to move the needle without interrupting the target surface and
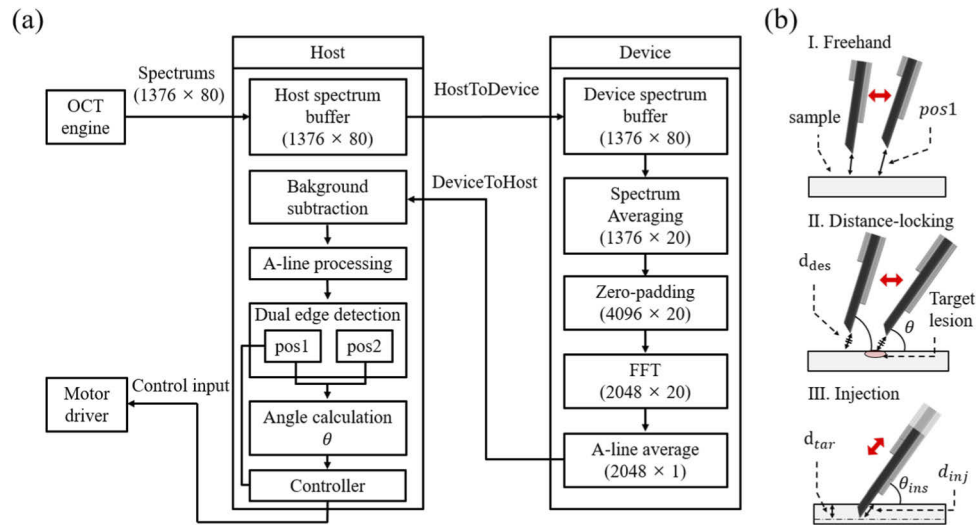
Fig. 4. (a) Flow chart and (b) schematic of three different operating modes of the two parallel CP-OCT fibers attached SMART system.

safely move and tilt the needle towards the lesion to be injected. The final mode is injection, and the needle is located beneath the surface of the target lesion to inject drugs. This shares the same control loop with the depth-locking mode so that hand tremor can be compensated; however, the target position of the control becomes different. When puncturing the sample, $pos1$ should have a negative value, whose amount is the injection depth denoted as d_{inj}.

During the injection, the target position of the control becomes $-d_{inj}$, which needs to be changed in accordance with the insertion angle, θ_{ins}, that is measured right before the needle is inserted to ensure constant target injection depth, d_{tar}, regardless of needle inclination. d_{tar} is a predetermined value such as the retinal thickness at the target lesion and is measured perpendicular to the surface of the corresponding area. In contrast, d_{inj} is the penetration depth along the insertion axis. Once d_{tar} is determined, d_{inj} is calculated using the following equation.

$$d_{inj} = d_{tar}/sin\theta_{ins} \tag{5}$$

Therefore, the more the needle is inclined, the larger the amount of d_{inj} is employed to produce a higher injection depth, i.e., injection depth correction is. If it is not possible to measure the injection angle, the injection depth perpendicular to the surface of the target lesion cannot be corrected accordingly.

3. Results

3.1. Evaluation on control performance of distance-locking

First, a commercial eye model (FUNDUS-Globe model, BIONIKO) was used to analyze the performances for hand tremor compensation and angle measurement, as shown in Fig. 5(a). The sclera is punctured with a 23G surgical trocar, and the needle tip is inserted to measure the distance from the inner surface of the eye model. The overlapped numbers 1 and 2 on the eye model indicate the initial and final points, respectively. As shown in the right sub-figures in Fig. 5(a), the initial point yields an acute angle, and the other yields an obtuse angle. While tilting the needle from the initial point to the final point, tremor compensation is actuated, and the angle is simultaneously calculated and recorded, as shown in Figs. 5(b) and (c). Before turning the control on, the hand tremors were captured; however, they were significantly reduced

during the control, as indicated by the red line, *pos*1, in Fig. 5(b). While tilting the needle, the shifted value of *pos*2 is observed owing to the curvature of the eye, which can provide intuitive information about the angle changes. The measured angle is shown in Fig. 5(c). As expected, the angle from the initial point is acute, 42°, and the final point provides an obtuse angle, 118°. The angle is roughly changed because of manual tilting; however, the position of the needle tip is safely maintained at a distance of 500 μm from the inner surface of the eye model.
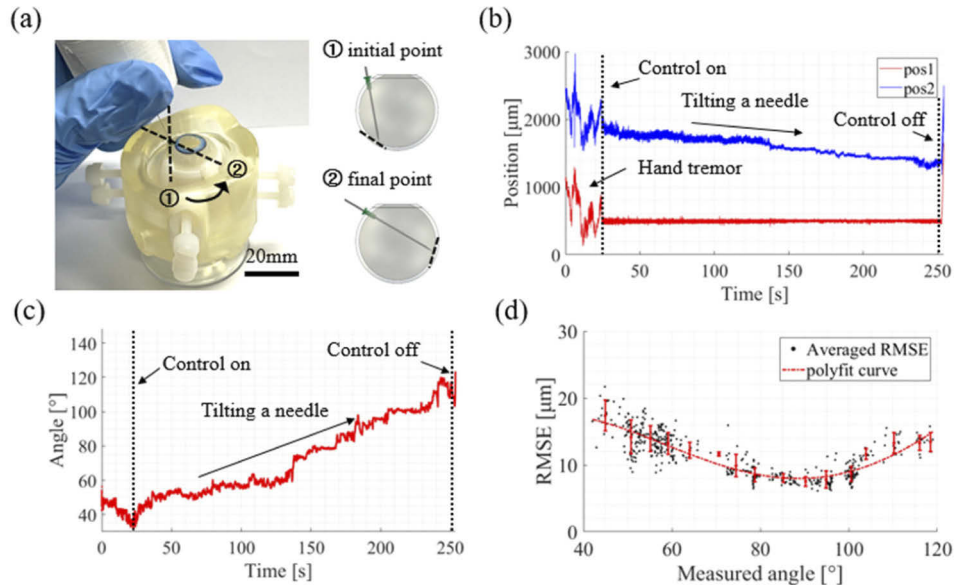
Fig. 5. Eye model test. (a) An experimental setup for hand-tremor reduction on an eye model, (b) and (c) acquired dual OCT signals and measured angle, respectively, and (d) the RMSE of data with respect to measured angle.

The control performance was evaluated by the RMSE values between *pos1* and the desired position, 500 μm. The temporally averaged RMSE for 0.5 s was continuously recorded with the angle at that time. When the needle is at an acute or obtuse angle from the sample,, the SNR of the A-line worsens so that it directly affects both the edge detection and control performance. Therefore, the RMSE must be analyzed for various angles; the distribution of the RMSE with respect to the measured angle is shown in Fig. 5(d). The black dots are the recorded RMSEs for every 0.5 s. They are averaged again with respect to the measured angle, and the stars and error bars correspond with the mean and standard deviation (std) of the RMSEs at the averaged angle. As indicated by the red dotted line, which is a poly fitted result, a smaller RMSE is achieved at the measured angle of 90°. The averaged RMSE of 7.8 μm was achieved in this case; however, the performance was degraded for greater inclinations while producing the averaged RMSE of 17.5 μm. Nevertheless, the proposed design still offers affordable performance and prohibits the needle tip from touching the sample owing to the high resolution of the OCT sensor and high operation speed of 1 kHz.

3.2. Injection test on agarose phantom

To analyze the injection performance, an injection phantom was constructed, as shown in Fig. 6(a). A 3% agarose gel was formulated to mimic the retina in terms of Young's modulus [28,29] and was thinly sliced using a single-edge blade (DN-52, DORCE). One drop of indocyanine green (ICG) was placed on the agar slice and spread to induce diffused reflection. Then, the sample was laid on a box made of polydimethylsiloxane (PDMS). Once the needle was inserted in the

agar slice, a small amount of the ICG permeates into the injection hole, resulting in a shadow on the PDMS box. Three different injections at insertion angles of 90°, 60°, and 45° were planned, as shown in Fig. 6(b), and d_{tar} is 270 μm, which is the general retinal thickness [23]. In the sample, the required injection depths, d_{inj}, are inscribed to assess placement of the needle tip at the desired d_{tar}. At 90°, d_{inj} is equal to d_{tar}. For needle inclinations of 60° and 45°, d_{inj} is set to 311.7 μm and 381.8 μm, respectively. Figures 6(c) and (d) are the injection results with injection depth correction. The three injections are performed consecutively on the same agar slice, and it is noted that *pos*1 has negative values during the injection. The magnified results are overlapped on the injection results and the RMSE errors for each injection are described. All three injections have smaller averaged RMSEs (5.67 μm, 6.65 μm, and 11.66 μm at 1st, 2nd, and 3rd injections) than those of distance-locking at each angle. The actual connection between the needle and agar slice would act as a damper such that the involuntary motion by hand tremor would decrease. In addition, injection depths were calculated at each insertion angle, and these coincided with the required values. The first injection was done at 90.9°, which had approximately same target depth, 270.03 μm. The second and third injections were performed at 60.1° and 46.4° by introducing injection depths of 311.4 μm and 372.8 μm, respectively; these various injection depths can be seen on the magnified view in Fig. 6(c). In the same manner, Figs. 6(e) and (f) are the results of the three injections without depth correction; the most distinguishable aspect here is that all injection depths were the same regardless of the insertion angles, in contrast to the results with injection depth correction. The injections were performed at insertion angles of 92.5°, 61.2°, and 42.5° with the same injection depth of 270 μm.

To validate whether the corrected injection depths could produce steady injections for oblique insertions, the cross-sectional profile of each injected case was imaged using a commercial SD-OCT (Callisto 930 nm OCT Imaging System, Thorlabs) after removing the ICG on the surface of the agar slice. It can be seen that steadier injection depths could be achieved by depth correction with precise injection angle measurements than without depth correction, as shown in Figs. 6(g) and (h), respectively. The perpendicular insertion has a similar injection depth for both cases; however, the depth uncorrected results produce shallow injections as the needle is inclined more. On the contrary, the depth-corrected injections are able to place the needle tip at constant depths in all cases.

3.3. Ex-vivo test on porcine eye

As an ex-vivo test, a porcine eye is excised, as shown in Fig. 7(a), and the microscopic view is overlapped on it. The microscopic images are displayed during the operation to visualize the injection lesion. Figures 7(b) and (c) are the measurements of the positions and angles during the ex-vivo test. The three operating modes are clearly seen: freehand, distance-locking, and injection. The measured positions for each mode are magnified and the RMSEs were calculated as 142.22 μm, 15.19 μm, and 12.72 μm, respectively. As expected, the injection RMSE was smaller than that of depth-locking, and the needle was supposed to be 45° for oblique insertion to the target depth of 220 μm. The actual injection, however, was performed at 43.3° and induced a d_{inj} of 320.7 μm. The needle tip was placed within the subretinal space for approximately 13 s, and a small dose of the ICG was injected using the connected syringe. Figure 7(d) shows a 3-dimensionally reconstructed SD-OCT image of an intact area on the porcine eye. The distinct features, such as choroid, inner limiting membrane (ILM), and RPE, can be visualized as shown by the yellow arrows. The injection aims to perfuse the ICG inside the subretinal space on the RPE layer, which is located between the photoreceptor (PR) layer and Bruch's membrane (BM) on a choroid.

Figure 7(e) shows the image of the injected lesion that is adjacent to the intact area in Fig. 7(d). Similar retinal features can be observed; however, there are apparent differences in the injected area. First, the trace of incision by the needle is revealed, as indicated by the dashed yellow lines.
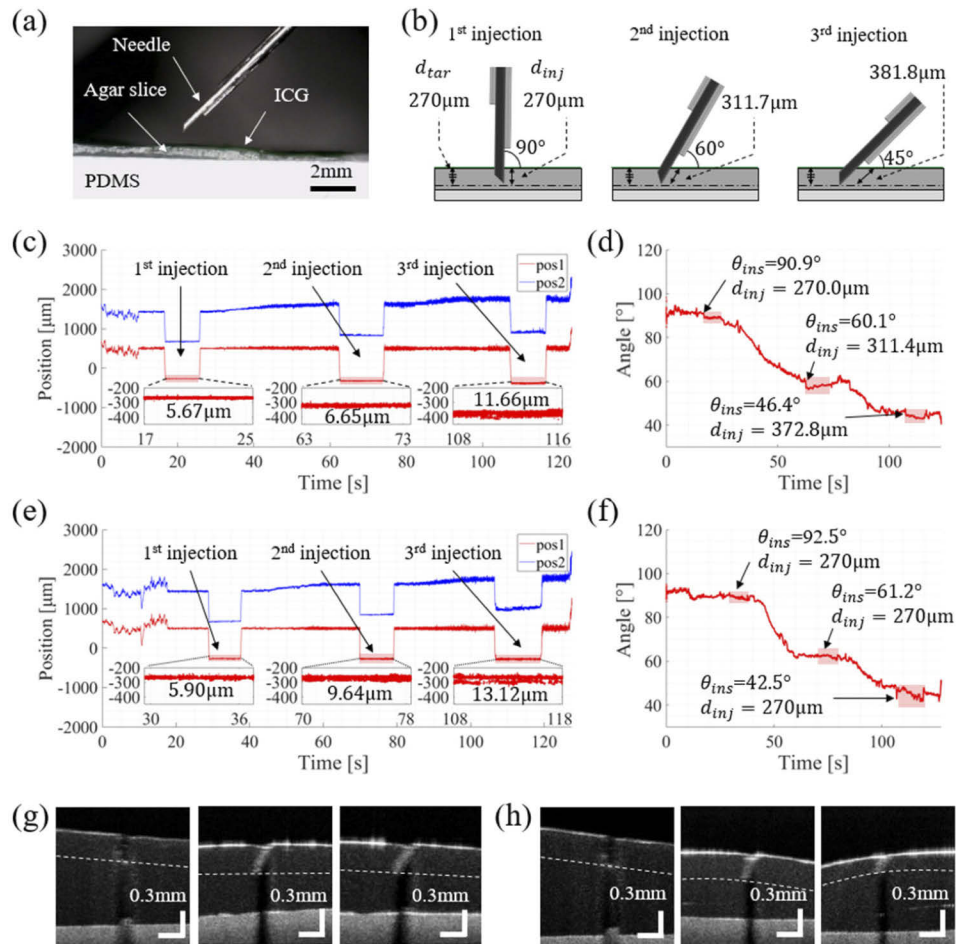
Fig. 6. Injection phantom test. (a) Optical image of an injection experiment on a phantom and the needle used; (b) schematics of the three injection cases; (c) and (d) results of the positions and angles with injection depth correction; (e) and (f) without injection depth correction; (g) and (h) SD-OCT images of the injected phantom with and without depth correction, respectively.
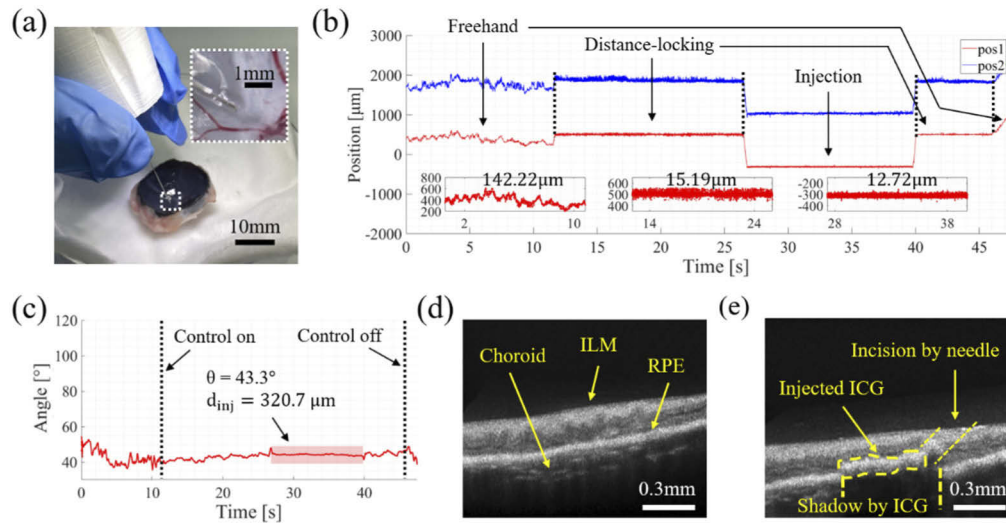
Fig. 7. (a) Experimental setup for injection of porcine eye; (b) and (c) measured position and angle, respectively; (d) and (e) part of the 3D OCT image of an intact area and injected lesion on the porcine eye, respectively (see Visualization 1).

The insertion angle is measured to be 43.3°, and the corresponding image is obtained. Second, the injected ICG can be clearly seen, and it is located on the RPE layer because the neighboring RPE layer is below that. Finally, a shadow is created by the high reflectivity of the ICG, so that it is impossible to see the cross-sectional image beyond the injected ICG. If the injection depth is not sufficient to reach the desired layer, most of the ICG cannot be transferred to the RPE. With the hand tremor compensation and injection depth correction, the subretinal injection was successfully performed to the target layer without damaging the retina of the porcine eye.

4.　Discussion and conclusion

In this study, two parallel CP-OCT fibers were attached to the needle of the SMART injector to calculate the insertion angle from the sample. The capacity for angle measurement is dependent on the laser specification and fiber configuration with the needle. The geometrical properties of two parallel beams based on the target sample were considered to design a mathematical model to calculate the angle. To achieve more precise angle calculations, the calibration and optimization procedures were performed using a rotational stage and microscope. The presented system is able to detect both the position and angle of the needle from the target simultaneously and compensate for an additionally required injection depth when oblique insertion of the needle is needed.

　In conclusion, steady injection depths could be achieved by injection depth correction with precise injection angle measurements using two parallel CP-OCT sensors attached to the SMART injector. The proof of concept for the two parallel beams in terms of angle measurement has already been proven in industrial applications, such as stage calibration. Through this work, we have proved that this structure can be minimized further by incorporating an all-fiber setup and can be further developed to miniaturize the probe-type angle measurement system, which is not only suitable for industrial measurements but also usable in biomedical or microsurgical applications. The proposed method has an intrinsic hypothesis that the surface of the sample between two measurement points is flat. In other words, it is impossible to measure the drastic changes of an angle within two measurement points, d_{c2c}. Nevertheless, it was possible to successfully measure angles on several samples such as an eye model and a porcine eye which are

flat enough within the two measurement points. Therefore, our system is capable of measuring the angle under the assumption that the distance between the two measurement points is larger than that of the irregular surface. Furthermore, it is possible to observe the overview structures of a target by increasing the number of optical fibers, which can enable measurement of the pitch as well as roll angles. Translational works to employ this angle measurement system to injection tasks are underway and expected to be implemented to other surgical applications, such as cannulation of veins or submucosa of internal organs.

Disclosures. The authors declare no conflicts of interest.

References

1. B. G. Ballios, M. J. Cooke, D. Van der Kooy, and M. S. Shoichet, "A hydrogel-based stem cell delivery system to treat retinal degenerative diseases," Biomaterials **31**(9), 2555–2564 (2010).
2. K. Shintani, D. L. Shechtman, and A. S. Gurwood, "Review and update: current treatment trends for patients with retinitis pigmentosa," J. Am. Optom. Assoc. **80**(7), 384–401 (2009).
3. J. R. Chao, D. A. Lamba, T. Klesert, K. Sternhagen, R. Taylor, A. Yanagida, and T. A. Reh, "Transplantation of human embryonic stem cell-derived retinal cells into the subretinal space of a non-human primate," Investig. Ophthalmol. Vis. Sci. **53**(14), 5839 (2012).
4. G. Yiu, S. H. Chung, I. N. Mollhoff, U. T. Nguyen, S. M. Thomasy, J. Yoo, and G. Noronha, "Suprachoroidal and subretinal injections of AAV using transscleral microneedles for retinal gene delivery in nonhuman primates," Mol. Ther.–Methods Clin. Dev. **16**, 179–191 (2020).
5. S. Russell, J. Bennett, J. A. Wellman, D. C. Chung, Z. F. Yu, A. Tillman, and D. Cross, "Efficacy and safety of voretigene neparvovec (AAV2-hRPE65v2) in patients with RPE65-mediated inherited retinal dystrophy: a randomised, controlled, open-label, phase 3 trial," Lancet **390**(10097), 849–860 (2017).
6. M. Zhou, Q. Yu, K. Huang, S. Mahov, A. Eslami, M. Maier, and M. A. Nasseri, "Towards Robotic-Assisted Subretinal Injection: A Hybrid Parallel–Serial Robot System Design and Preliminary Evaluation," IEEE Trans. Ind. Electron. **67**(8), 6617–6628 (2020).
7. S. Olivier, D. R. Chow, K. H. Packo, M. W. MacCumber, and C. C. Awh, "Subretinal recombinant tissue plasminogen activator injection and pneumatic displacement of thick submacular hemorrhage in age-related macular degeneration," Ophthalmology **111**(6), 1201–1208 (2004).
8. K. Xue, M. Groppe, A. P. Salvetti, and R. E. MacLaren, "Technique of retinal gene therapy: delivery of viral vector into the subretinal space," Eye **31**(9), 1308–1316 (2017).
9. T. Nakano, N. Sugita, T. Ueta, Y. Tamaki, and M. Mitsuishi, "A parallel robot to assist vitreoretinal surgery," Int. J. CARS **4**(6), 517–526 (2009).
10. J. P. Ehlers, S. K. Srivastava, D. Feiler, A. I. Noonan, A. M. Rollins, and Y. K. Tao, "Integrative advances for OCT-guided ophthalmic surgery and intraoperative OCT: microscope integration, surgical instrumentation, and heads-up display surgeon feedback," PLoS One **9**(8), e105224 (2014).
11. Y. S. You, C. Y. Lee, C. Li, S. H. Lee, K. Kim, and H. Jung, "An arched micro-injector (ARCMI) for innocuous subretinal injection," PLoS One **9**(8), e104145 (2014).
12. Y. Ma, C. Lee, C. G. Li, Y. S. You, H. L. Sung, and H. Jung, "Minimally invasive curved-micro-drainer (CMD) capable of innocuous drainage of subretinal fluid for the treatment of retinal detachment," Biomed. Microdevices **18**(4), 65 (2016).
13. W. Wei, C. Popplewell, S. Chang, H. F. Fine, and N. Simaan, "Enabling technology for microvascular stenting in ophthalmic surgery," J. Med. Devices **4**(1), 014503 (2010).
14. P. S. Jensen, K. W. Grace, R. Attariwala, J. E. Colgate, and M. R. Glucksberg, "Toward robot-assisted vascular microsurgery in the retina," Graefe's Arch. Clin. Exp. Ophthalmol. **235**(11), 696–701 (1997).
15. C. N. Riviere and P. S. Jensen, "A study of instrument motion in retinal microsurgery," In *Proceedings of the 22nd Annual International Conference of the IEEE Engineering in Medicine and Biology Society* (2000), pp. 59–60.
16. B. C. Becker, R. A. MacLachlan, L. A. Lobes Jr, and C. N. Riviere, "Semiautomated intraocular laser surgery using handheld instruments," Lasers Surg. Med. **42**(3), 264–273 (2010).
17. S. Mukherjee, S. Yang, R. A. MacLachlan, L. A. Lobes, J. N. Martel, and C. N. Riviere, "Toward monocular camera-guided retinal vein cannulation with an actively stabilized handheld robot," *2017 IEEE International Conference on Robotics and Automation* (ICRA, 2017), pp. 2951–2956.

18. D. Huang, E. A. Swanson, C. P. Lin, J. S. Schuman, W. G. Stinson, W. Chang, and C. A. Puliafito, "Optical coherence tomography," Science **254**(5035), 1178–1181 (1991).

19. C. Song, P. L. Gehlbach, and J. U. Kang, "Active tremor cancellation by a "smart" handheld vitreoretinal microsurgical tool using swept source optical coherence tomography," Opt. Express **20**(21), 23414–23421 (2012).

20. C. Song, D. Y. Park, P. L. Gehlbach, S. J. Park, and J. U. Kang, "Fiber-optic OCT sensor guided "SMART" micro-forceps for microsurgery," Biomed. Opt. Express **4**(7), 1045–1050 (2013).

21. D. Koo, H. C. Park, P. L. Gehlbach, and C. Song, "Development and preliminary results of bimanual smart micro-surgical system using a ball-lens coupled OCT distance sensor," Biomed. Opt. Express **7**(11), 4816–4826 (2016).

22. J. U. Kang and G. W. Cheon, "Demonstration of subretinal injection using common-path swept source OCT guided microinjector," Appl. Sci. **8**(8), 1287 (2018).

23. A. M. Bagci, M. Shahidi, R. Ansari, M. Blair, N. P. Blair, and R. Zelkha, "Thickness profiles of retinal layers by optical coherence tomography image segmentation," Am. J. Ophthalmol. **146**(5), 679–687.e1 (2008).

24. S. R. Gillmer, R. C. G. Smith, S. C. Woody, and J. D. Ellis, "Compact fiber-coupled three degree-of-freedom displacement interferometry for nanopositioning stage calibration," Meas. Sci. Technol. **25**(7), 075205 (2014).

25. H. Yan, H. Z. Duan, L. T. Li, Y. R. Liang, J. Luo, and H. C. Yeh, "A dual-heterodyne laser interferometer for simultaneous measurement of linear and angular displacements," Rev. Sci. Instrum. **86**(12), 123102 (2015).

26. C. Yeo, H. C. Park, S. Jang, P. L. Gehlbach, and C. Song, "Dual optical coherence tomography sensor guided, two-motor, horizontal SMART micro-scissors," Opt. Lett. **41**(20), 4723–4726 (2016).

27. K. Zhang, W. Wang, J. Han, and J. U. Kang, "A surface topology and motion compensation system for microsurgery guidance and intervention based on common-path optical coherence tomography," IEEE Trans. Biomed. Eng. **56**(9), 2318–2321 (2009).

28. I. L. Jones, M. Warner, and J. D. Stevens, "Mathematical modelling of the elastic properties of retina: a determination of Young's modulus," Eye **6**(6), 556–559 (1992).

29. B. Luo, R. Yang, P. Ying, M. Awad, M. Choti, and R. Taylor, "Elasticity and echogenicity analysis of agarose phantoms mimicking liver tumors," In *Proceedings of the IEEE 32nd Annual Northeast Bioengineering Conference* (2006), pp. 81–82.